The Astrophysical Journal, 824:138 (12pp), 2016 June 20 doi:10.3847/0004-637X/824/2/138

THE WIND NEBULA AROUND MAGNETAR SWIFT J1834.9–0846

G. Younes[1], C. Kouveliotou[1], O. Kargaltsev[1], R. Gill[2], J. Granot[2], A. L. Watts[3], J. Gelfand[4], M. G. Baring[5], A. Harding[6], G. G. Pavlov[7], A. J. van der Horst[1], D. Huppenkothen[8,9], E. Göğüş[10], L. Lin[11], and O. J. Roberts[12]
[1] Department of Physics, The George Washington University, Washington, DC 20052, USA
[2] Department of Natural Sciences, The Open University of Israel, 1 University Road, P.O. Box 808, Raánana 43537, Israel
[3] Astronomical Institute "Anton Pannekoek," University of Amsterdam, Postbus 94249, 1090 GE Amsterdam, The Netherlands
[4] NYU Abu Dhabi, P.O. Box 903, New York, NY 10276, USA
[5] Department of Physics and Astronomy, Rice University, MS-108, P.O. Box 1892, Houston, TX 77251, USA
[6] Astrophysics Science Division, NASA Goddard Space Flight Center, Greenbelt, MD 20771, USA
[7] Department of Astronomy & Astrophysics, Pennsylvania State University, 525 Davey Lab, University Park, PA 16802, USA
[8] Center for Data Science, New York University, 726 Broadway, 7th Floor, New York, NY 10003, USA
[9] Center for Cosmology and Particle Physics, Department of Physics, New York University, 4 Washington Place, New York, NY 10003, USA
[10] Sabancı University, Orhanlı-Tuzla, İstanbul 34956, Turkey
[11] Department of Astronomy, Beijing Normal University, Beijing, 100875, China
[12] School of Physics, University College Dublin, Stillorgan Road, Belfield, Dublin 4, Ireland
Received 2016 February 24; revised 2016 April 13; accepted 2016 April 18; published 2016 June 21

ABSTRACT

We report on the analysis of two deep *XMM-Newton* observations of the magnetar Swift J1834.9−0846 and its surrounding extended emission taken in 2014 March and October, 2.5 and 3.1 yr after the source went into outburst. The magnetar is only weakly detected in the first observation, with an absorption-corrected flux $F_{0.5-10\,\mathrm{keV}} \approx 4 \times 10^{-14}\,\mathrm{erg\,s^{-1}\,cm^{-2}}$ and a 3σ upper limit during the second observation of about 3×10^{-14} $\mathrm{erg\,s^{-1}\,cm^{-2}}$. This flux level is more than 3 orders of magnitude lower than the flux measured at the outburst onset in 2011 September. The extended emission, centered at the magnetar position and elongated toward the southwest, is clearly seen in both observations; it is best fit by a highly absorbed power law (PL), with a hydrogen column density of $N_{\mathrm{H}} = 8.0 \times 10^{22}\,\mathrm{cm^{-2}}$ and PL photon index $\Gamma = 2.2 \pm 0.2$. Its flux is constant between the two observations at $F_{0.5-10\,\mathrm{keV}} = 1.3 \times 10^{-12}\,\mathrm{erg\,s^{-1}\,cm^{-2}}$. We find no statistically significant changes in the spectral shape or the flux of this extended emission over a period of 9 yr from 2005 to 2014. These new results strongly support the extended emission nature as a wind nebula and firmly establish Swift J1834.9−0846 as the first magnetar to show a surrounding wind nebula. Further, our results imply that such nebulae are no longer exclusive to rotation-powered pulsars and narrow the gap between these two subpopulations of isolated neutron stars. The size and spectrum of the nebula are compatible with those of pulsar-wind nebulae, but its radiative efficiency $\eta_{\mathrm{X}} = L_{\mathrm{X}}/\dot{E} \approx 0.1$ is markedly high, possibly pointing to an additional wind component in Swift J1834.9−0846.

Key words: stars: individual (Swift J1834.9–0846) – stars: magnetars – stars: neutron – X-rays: ISM

1. INTRODUCTION

Magnetars represent a subclass of isolated neutron stars (NSs) with a unique set of observational properties. They often have long spin periods ($P \sim 2$–12 s) and large spin-down rates ($\dot{P} \sim 10^{-13}$–10^{-10}). They are usually observed as bright X-ray sources with luminosities $L_{\mathrm{X}} \sim 10^{32}$–$10^{36}\,\mathrm{erg\,s^{-1}}$, larger than their corresponding rotational energy losses $(-\dot{E}_{\mathrm{rot}} = (2\pi)^2 I\dot{P}/P^3 \sim 10^{30}$–$10^{35}\,\mathrm{erg\,s^{-1}}$, where I is the NS moment of inertia, $I \approx 10^{45}\,\mathrm{g\,cm^2}$). Almost all have been observed to emit short (~0.1 s), bright ($E_{\mathrm{burst}} \sim 10^{37}$–$10^{40}$ erg), hard X-ray bursts (see Mereghetti et al. 2015; Turolla et al. 2015, for reviews). Assuming dipole braking, the majority of magnetar timing properties indicate strong surface dipole magnetic fields ($B \gtrsim B_{\mathrm{crit}}$, where $B_{\mathrm{crit}} = 4.4 \times 10^{13}$ G is the electron quantum critical field), while their internal magnetic fields are thought to be even larger (Thompson & Duncan 1995). The decay of their internal and external magnetic fields represents their dominant energy reservoir, powering their persistent emission, as well as their bursting activity (Thompson & Duncan 1995, 1996; Thompson et al. 2002; Beloborodov 2009; Dall'Osso et al. 2012). Finally, a few magnetars have also shown pulsed radio emission (Camilo et al. 2006, 2007; Rea et al. 2012; Torne et al. 2015).

In the past decade, several observational results have demonstrated that the above properties are neither exclusively seen in magnetars nor solely attributed to superstrong surface dipole fields ($B \gtrsim B_{\mathrm{crit}}$). For the purposes of this study, we single out below two of these results.

PSR J1846−0258 is a 0.3 s rotation-powered pulsar (RPP) located inside the supernova remnant (SNR) Kes 75. Its spin-down rate implies a surface dipole magnetic field $B = 4.9 \times 10^{13}$ G, on the boundary between RPPs and classical magnetars (Gotthelf et al. 2000). Unlike magnetars, however, PSR J1846−0258 has a large rotational energy loss rate, $\dot{E} = 8.1 \times 10^{36}\,\mathrm{erg\,s^{-1}}$, well above its persistent X-ray luminosity, $L_{\mathrm{X}} = 4.1 \times 10^{34}\,\mathrm{erg\,s^{-1}}$. Its rotational energy loss also powers a bright pulsar wind nebula (PWN), $L_{\mathrm{X,PWN}} = 1.4 \times 10^{35}\,\mathrm{erg\,s^{-1}}$, with an X-ray efficiency $\eta_{\mathrm{PWN}} = L_{\mathrm{X}}/\dot{E} = 2\%$, somewhat high but not unusual for a young RPP (Ng et al. 2008). The source spin-down age is $\tau = P/(n-1)\dot{P} = 884$ yr for a measured breaking index of $n = 2.65$ (Livingstone et al. 2006). Gavriil et al. (2008)

reported the discovery of short hard X-ray bursts from PSR J1846−0258, a trademark of typical magnetar sources. The bursts were accompanied by flux enhancement and timing noise, also typical properties of magnetars. These observational results demonstrated that an otherwise typical RPP can in fact show typical magnetar properties, bridging the gap between the two NS subpopulations.

The discovery in 2009 of SGR J0418+5729 strengthened the above conclusion. The source was detected after it emitted two short hard X-ray bursts (van der Horst et al. 2010), and exhibited typical magnetar-like properties: a period of ∼9 s, X-ray flux enhancement soon after the bursts, and a quasi-exponential flux decay in the following months (Esposito et al. 2010; Rea et al. 2013). A spin-down rate could only be measured after 3 yr of observations, and it was found to be the lowest of any magnetar, $\dot{P} = 4 \times 10^{-15}$ s s^{-1}, implying a surface dipole field $B = 6 \times 10^{12}$ G (Rea et al. 2010). This field is well within the range of regular RPPs, indicating that a strong dipole field is not a requirement for displaying magnetar-like properties in an isolated NS.

While the above observational results demonstrate a possible link between RPPs and magnetars, there exists one RPP property, which has not thus far been identified in a typical magnetar. Most RPPs possess a large rotational energy loss rate that powers a relativistic particle wind, often seen as a PWN, whose X-ray emission is the result of synchrotron radiation of the shocked wind (Gaensler & Slane 2006; Kaspi et al. 2006; Kargaltsev & Pavlov 2008). Magnetars, on the other hand, have rotational energy loss rates on average about 2 orders of magnitude smaller than RPPs (although with some overlap in their distributions; Olausen & Kaspi 2014), making the production of a rotationally powered nebula less likely. Magnetars, however, are thought to produce particle outflows, either steady or released during bursting episodes (Harding et al. 1996, 1999; Thompson & Blaes 1998; Tong et al. 2013), for which the only observational examples are the transient radio emissions detected from SGR 1900+14 and SGR 1806 −20 following their 1999 and 2004 giant flares, respectively (Frail et al. 1999; Gaensler et al. 2005).

Swift J1834.9−0846 is a typical magnetar, discovered on 2011 August 7, when it emitted a short hard X-ray burst. Follow-up X-ray observations revealed a spin period $P = 2.48$ s and a spin-down rate $\dot{P} = 7.96 \times 10^{-12}$ s s^{-1}, implying a surface dipole magnetar field strength $B = 1.4 \times 10^{14}$ G (at the equator) and a rotational energy loss rate $\dot{E}_{\rm rot} = 2.1 \times 10^{34}$ erg s^{-1}. Following the burst, the source X-ray flux increased by more than 3 orders of magnitude and decayed quasi-exponentially in the following months (Kargaltsev et al. 2012; Esposito et al. 2013). *XMM-Newton* observations of Swift J1834.9−0846 in 2011, a month after the source went into outburst, showed a very unusual extended emission around the magnetar (Younes et al. 2012, hereafter Y12). This emission, centered at the source position, was asymmetrical, extending to the southwest of the magnetar. Moreover, the same extended emission was detected in an archival *XMM-Newton* observation 6 yr earlier at a similar flux level (albeit with large uncertainties), while the magnetar was ∼23 times fainter (Y12). Due to the above unusual properties, Y12 conjectured that this extended emission might be a wind nebula powered by the magnetar. Esposito et al. (2013) later argued that this emission was a dust scattering halo occurring in a giant molecular cloud (GMC) located along the line of sight (Tian et al. 2007). They suggested that a previous outburst from the source prior to 2005 might be responsible for its earlier detection. The asymmetrical shape was attributed to nonuniformity in the dust distribution.

Table 1
Log of the *XMM-Newton* Observations

Observation ID	Date	Instrument	Good Time Intervals (ks)
0723270101	2014 Mar 16	PN	70.0
	2014 Mar 16	MOS1	87.7
	2014 Mar 16	MOS2	88.5
0743020201	2014 Oct 16	PN	60.0
	2014 Oct 16	MOS1	78.0
	2014 Oct 16	MOS2	77.7

In this paper, we report on the analysis of two deep *XMM-Newton* observations of Swift J1834.9−0846 and its associated extended emission taken in 2014 March and in 2014 October, 2.5 and 3.1 yr after the source went into outburst. We present the observations and data reduction in Section 2, and we report our analysis results in Section 3. We discuss our findings in Section 4. We assume that Swift J1834.9−0846 is at a distance of $d = 4\ D_{4\,\rm kpc}$ considering a likely association with the SNR W41, given its location at the geometrical center of the remnant (Tian et al. 2007; Leahy & Tian 2008).

2. OBSERVATIONS AND DATA REDUCTION

We observed Swift J1834.9−0846 with *XMM-Newton* on two different dates. The first observation started on 2014 March 16, for a total exposure of 94.9 ks. The second observation took place 7 months later, on 2014 October 16, for a total of 85.0 ks. During both observations, the EPIC-PN (Strüder et al. 2001) camera operated in extended full-frame mode, using the medium filter, while the MOS cameras operated in full-frame mode. We used the Science Analysis System (SAS) version 14.0.0, and HEASOFT version 6.16 for the reduction and analysis of all data products. Data were selected using event patterns 0−4 and 0−12 for the PN and MOS cameras, respectively, during only good X-ray events ("FLAG = 0"). For both observations, we excluded intervals of enhanced particle background, only accepting those for which the count rate above 10 keV for the entire PN and MOS fields of view did not exceed 0.4 and 0.35 counts s^{-1}, respectively.[13] Table 1 lists the log of the two *XMM-Newton* observations.

To perform our spectral analysis, source events were extracted from specific regions as described in Section 3.2 and shown in Figure 1. Background events were extracted from a 5′-radius circle on the same CCD as the source, excluding point sources as derived from a source detection algorithm (Section 3.1). The task *backscale* was used to calculate the exact area of the source and background regions, correcting for excluded point sources, CCD gaps, and bad pixels. We generated response matrix files using the SAS task *rmfgen*, while ancillary response files were generated using the SAS task *arfgen*. All spectra were created in the energy range 0.5–10 keV.

XSPEC (Arnaud 1996) version 12.8.2 was used for our analysis. The photoelectric cross sections of Verner et al.

[13] http://xmm.esac.esa.int/sas/current/documentation/threads/EPIC_filterbackground.shtml

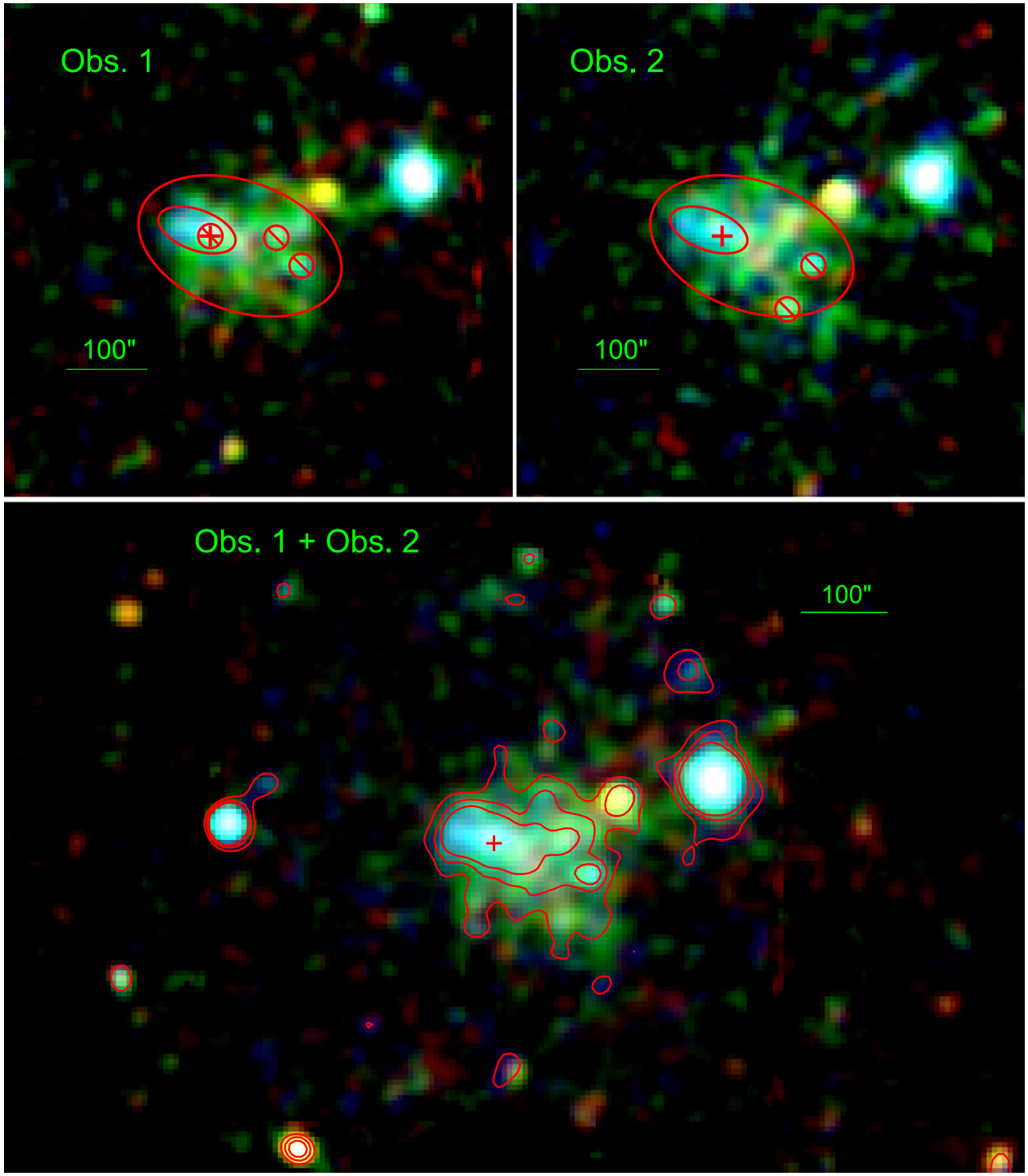

Figure 1. Upper panels: PN+MOS1+MOS2 exposure-map-corrected RGB images (2–3 keV in red, 3–4.5 keV in green, 4.5–10 keV in blue) of the extended emission around Swift J1834.9−0846 during obs. 1 (2014 March 16, left) and obs. 2 (2014 October 16, right). The red cross indicates the magnetar position, which is weakly detected in obs. 1 above the strong extended emission. The inner ($25'' \times 50''$ minor and major axes) and outer ($80'' \times 130''$ minor and major axes) ellipses are regions used to investigate spatial-spectral evolution within the nebula. Red crossed-out circles are weak point sources within the extended emission excluded from any imaging and spectral analyses. Lower panel: PN+MOS1+MOS2 combined images from the two observations. The contours are at the 2.5σ, 3.0σ, and 3.5σ levels. The red cross indicates the magnetar position. See text for more details.

(1996) and the abundances of Wilms et al. (2000) were used to account for absorption by neutral gas. For all spectral fits using all three cameras of the EPIC detector, we added a multiplicative constant normalization, frozen to 1 for the PN and allowed to vary for MOS1 and MOS2, to take into account any calibration uncertainties between the three instruments. We found a 3%–5% variation in the MOS1 and MOS2 normalizations relative to PN. All quoted uncertainties in this study are at the 1σ level, unless otherwise noted.

3. RESULTS

3.1. Imaging Analysis

We used the *images* script[14] to produce a cleaned image of the nebula for both *XMM-Newton* observations. This script uses raw event data files and filters for high background intervals, removes bad pixels and columns, corrects for several camera inefficiencies through an exposure map, and, finally, merges PN and MOS data. The script allows the production of these images in different energy bands, using a specified pixel binning and smoothing radius. Figure 1 shows the results of the script for observation 0723270101 (obs. 1 hereinafter, upper left panel) and 0743020201 (obs. 2 hereinafter, upper right panel). We use three energy bands to produce these images, 2–3 keV (red), 3–4.5 keV (green), and 4.5–10 keV (blue). The 2 keV lower limit was set because the source is highly absorbed, and hence data below 2 keV are mostly due to foreground noise. The images are also binned to 6″ pixel^{-1}and smoothed with an FWHM of 20″. The extended emission, clearly present in both images around the magnetar position (marked as a red cross), is remarkably similar in the two observations. We show in the lower panel of Figure 1 the merged images of the two observations of the extended emission with the 2.5σ, 3σ, and 3.5σ contours. This is the deepest image of the extended emission around the magnetar Swift J1834.9−0846.

Figure 1 shows a clear trend in hardness, with the inner part of the extended emission appearing harder than its outskirts. To identify and remove the contribution of any background (or foreground) point sources within the field of the extended emission, we ran two source detection algorithms. The `edetectchain`[15] uses an exposure-corrected image to look for sources within a 5 × 5 pixel box using a surrounding background of a 2 pixel box beyond the source in all input images (e.g., PN, MOS1, and MOS2) simultaneously. It then masks the sources found and creates a background map of the field of view through a 2D spline fit. Finally, using the values from this background map, it searches for sources within a 5 × 5 pixel box in all input images simultaneously. The `edetectchain` algorithm also performs point source or extended emission fits to each of the sources found through the task `emldetect`. The other detection algorithm we ran on the data (PN, MOS1, and MOS2 separately) is `wavdetect`.[16] This algorithm correlates a "Ricker wavelet" ("Mexican Hat wavelet") function to a given 2D image. Pixels with large positive correlation and a low significance ($<2 \times 10^{-6}$) are flagged as sources and removed from the data, and the same correlations are performed again until no more sources are found. This algorithm is developed for *Chandra* observations, but it can also be used with *XMM-Newton* data using the relevant exposure and point-spread function (PSF) map files.

Figure 2 shows the PN, MOS1, and MOS2 exposure-corrected combined images for obs. 1 (upper panels) and obs. 2 (lower panels) in the 2–10 keV range, along with the results from both source-detection algorithms. Both algorithms produce similar results, except that the `edetectchain` algorithm flags a source at the position of the magnetar in obs. 2, while the wavdetect algorithm does not. We note that the source detected using `edetectchain` at the magnetar position in both observations is flagged as extended. The faint X-ray sources detected in the two observations are likely weak X-ray transients (e.g., Asai et al. 1998; Campana et al. 1998), resulting in different source detections between obs. 1 and obs. 2.

To determine whether the magnetar emission is detected above the extended-emission level, we estimated the number of counts and computed the hardness ratios (HRs) in both observations. Using the PN camera in the range 2–10 keV, we estimate the background-corrected number of counts in a circle with radius 20″ (75% encircled energy) around the magnetar position (Kargaltsev et al. 2012). Normalizing by the good-time intervals in both observations and correcting for bad pixels and CCD gaps, we find 245 ± 9 counts and 196 ± 11 counts for obs. 1 and obs. 2, respectively. The difference of 49 ± 14 counts between the two observations represents a 3.5σ significance. Moreover, the radial profiles of the two observations in the 2–10 keV range (Figure 3) centered at the magnetar position (Kargaltsev et al. 2012) reveal a central excess emission in obs. 1 compared to obs. 2. Beyond a few arcseconds, the radial profiles from both observations are similar. We conclude that there is a 3.5σ count excess around the magnetar position in obs. 1.

We estimate the HR ($HB_{4.5-10\,keV}/SB_{2-4.5\,keV}$) within the 20″ circle by first estimating the photon flux in the two energy bands for all instruments separately. The photon flux is estimated by correcting the number of counts observed within the 20″ circle for CCD gaps and bad pixels and then normalizing by the "LIVETIME" exposure and the average detector effective area at the source location in the given energy band. Finally, we subtracted the background contribution from these photon fluxes using the background region as described in Section 2. The photon fluxes in the different energy bands and the HRs for obs. 1 and obs. 2 are shown in Table 2.

We also derived the HRs of two other regions within the extended emission following the same method as above. The first region, hereafter the inner ellipse, is indicated by the smaller red ellipse in Figure 1, and the second region, hereafter the outer ellipse, is indicated by the larger red ellipse. These elliptical regions were defined according to their spectral appearance in the image. Point sources within each of these two regions (defined as crossed-out circles with 15″ radii), as derived from the source detection algorithms, are excluded. The magnetar (shown as a red circle with a 20″ radius) was excluded from the inner ellipse, and the inner ellipse was excluded from the outer ellipse. These photon fluxes and HRs for obs. 1 and obs. 2 are shown in Table 2.

Two interesting conclusions can be drawn from the results in Table 2. First, the HR in a 20″ circle around the magnetar position indicates a softer spectrum in obs. 1 than in obs. 2. Moreover, the HR around the magnetar position in obs. 2 is almost identical to the HR in the inner ellipse of the two observations. Hence, given the central excess counts in obs. 1 compared to obs. 2 and the softer spectrum, we conclude that the magnetar is weakly detected in obs. 1, while it has faded as indicated by the harder extended emission during obs. 2. Second, the HR of the outer ellipse is noticeably smaller than the HR of the inner ellipse, indicating spectral softening with increasing distance from the magnetar position.

[14] http://xmm.esac.esa.int/external/xmm_science/gallery/utils/images.shtml
[15] http://xmm.esac.esa.int/sas/current/doc/edetect_chain/edetect_chain.html
[16] http://cxc.harvard.edu/ciao/threads/wavdetect/

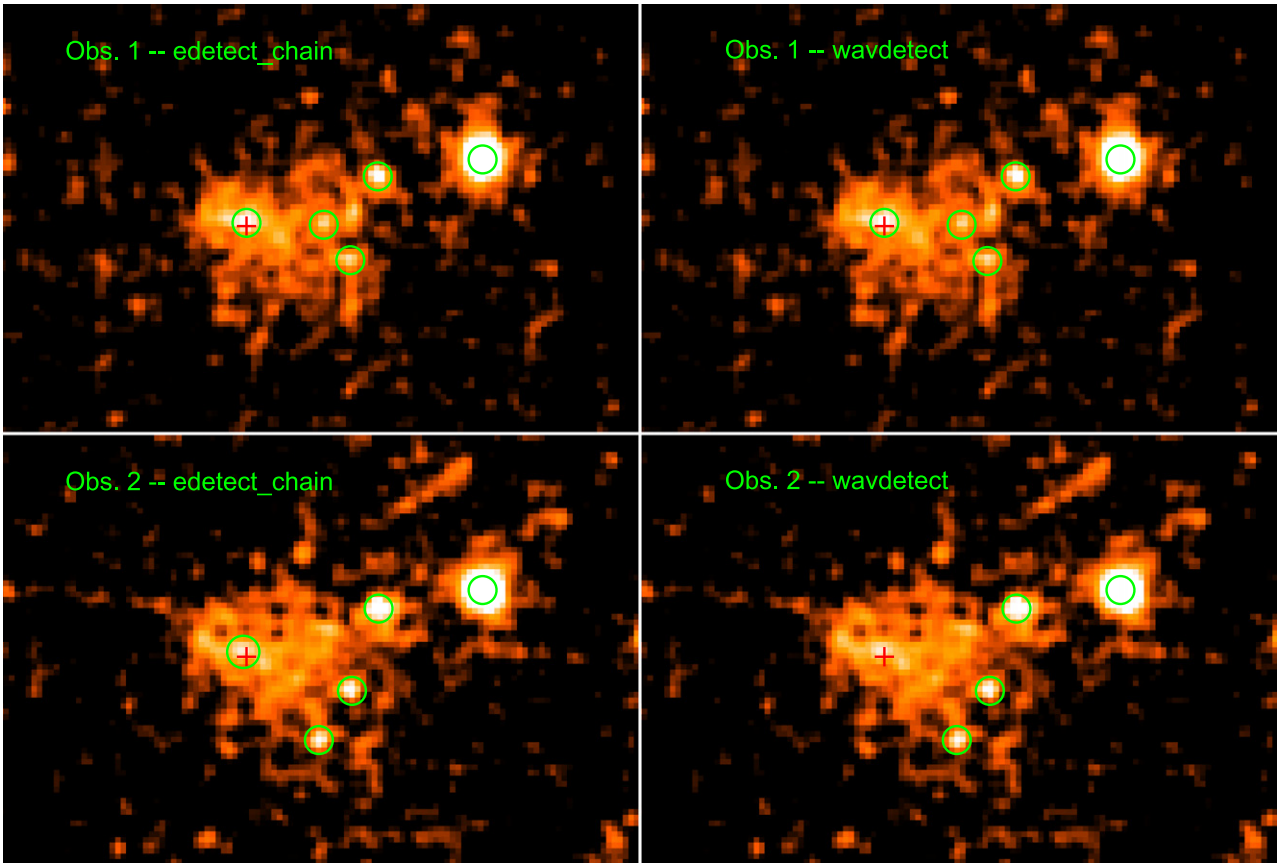

Figure 2. *XMM-Newton* EPIC images in the 2–10 keV band, Gaussian smoothed with an FWHM of 12″. Upper panels: obs. 1 image with the results from the source detection algorithm `edetectchain` (left) and `wavdetect` (right) overlaid. Lower panels: obs. 2 image with the results from the source detection algorithm `edetectchain` (left) and `wavdetect` (right) overlaid. The position of Swift J1834.9−0846 is marked as a red cross in all panels. The difference in the point sources detected between the two observations is likely the result of weak X-ray transients.

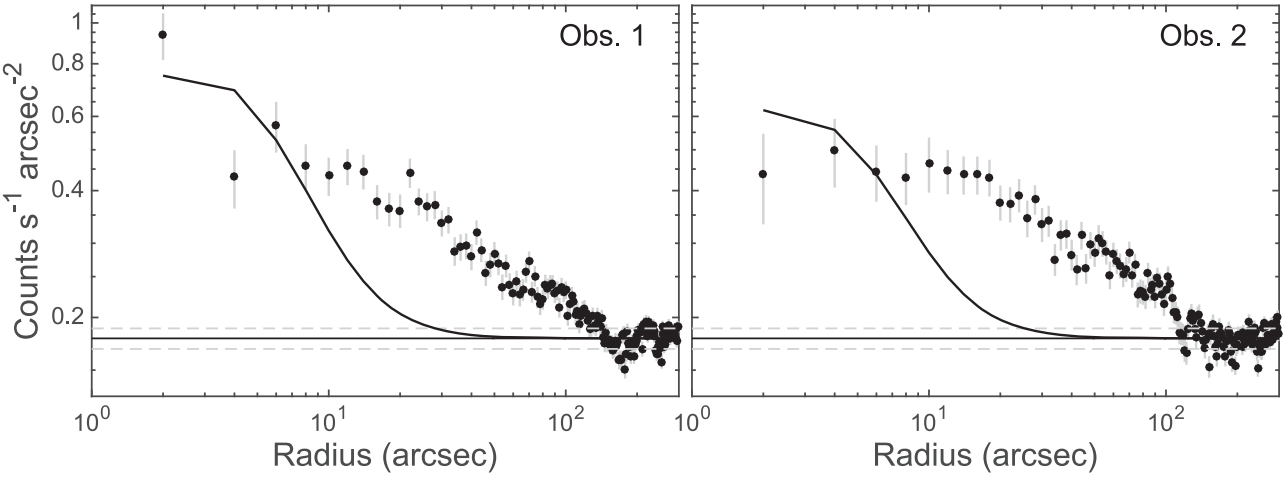

Figure 3. The 2–10 keV radial profiles from *XMM-Newton* obs. 1 (left panel) and obs. 2 (right panel) centered on the position of Swift J1834.9−0846. The profile of obs. 1 is normalized to have the same background level as obs. 2 (shown as a horizontal black solid line, with its 1σ deviation as gray dashed lines). The average PSF from all three EPIC instruments for a point source at the magnetar position is also shown. See text for details.

3.2. Spectral Analysis

We extracted the source spectra from the area within the big ellipse (80″ × 130″) in Figure 1 (upper panels), excluding the point sources detected in each observation. The background spectrum is extracted from a region as defined in Section 2. We then subtracted the background spectrum from the source emission spectrum, as is usually done for point sources. This approach should be valid for our case since the extent of the emission is too small to cause any strong vignetting effects. We used the Cash statistic (C-stat in XSPEC) for our parameter estimation and grouped the spectra to have 5 counts per bin. We fit the PN, MOS1, and MOS2 spectra of obs. 1 and obs. 2

Table 2
Photon Fluxes and Hardness Ratios for Different Locations within the Extended Emission

Parameter	Photon Flux (2–4.5 keV) (10^{-6} photons cm^{-2} s^{-1})	Photon Flux (4.5–10 keV) (10^{-6} photons cm^{-2} s^{-1})	HR
Magnetar position (obs. 1)	3.0 ± 0.2	5.1 ± 0.5	1.7 ± 0.2
Magnetar position (obs. 2)	2.3 ± 0.2	5.5 ± 0.6	2.4 ± 0.3
Inner ellipse (obs. 1)	2.0 ± 0.2	4.7 ± 0.5	2.4 ± 0.4
Inner ellipse (obs. 2)	1.6 ± 0.2	4.3 ± 0.5	2.7 ± 0.5
Inner ellipse (average)	1.8 ± 0.1	4.5 ± 0.4	2.5 ± 0.3
Outer ellipse (obs. 1)	15.0 ± 1.0	13.4 ± 1.5	0.9 ± 0.1
Outer ellipse (obs. 2)	13.3 ± 0.7	10.9 ± 1.4	0.8 ± 0.1
Outer ellipse (average)	14.2 ± 0.6	12.2 ± 1.0	0.9 ± 0.1

simultaneously with an absorbed power-law (PL) model. We linked all parameters between the two observations assuming no variability in the extended emission.

We find a PL photon index $\Gamma = 2.2 \pm 0.2$ and an absorbing hydrogen column density $N_{\rm H} = 8.0^{+0.9}_{-0.8} \times 10^{22}\,{\rm cm}^{-2}$. Since we are using C-stat for parameter estimation, we used the XSPEC command `goodness`[17] to evaluate the goodness of fit. The `goodness` command simulates a user-defined number of spectra based on a Gaussian distribution of the best-fit model parameters. It derives the percentage of simulations with fit statistic lower than that for the data. In the case where the data are drawn from the model, this percentage should be around 50%. Simulating 10,000 realizations of our data based on the above best-fit model, we find that 57% of the simulated spectra have a fit statistic lower than the best-fit statistic, C-stat = 4210.82 for 4140 degrees of freedom (dof), implying that our simple model provides a good fit to the data.

We find an absorption-corrected 0.5–10 keV flux $F_{0.5-10\,{\rm keV}} = 1.3^{+0.4}_{-0.2} \times 10^{-12}$ erg s^{-1} cm^{-2}, which translates into a luminosity $L_{0.5-10\,{\rm keV}} = 2.5^{+0.7}_{-0.6} \times 10^{33}\ D^2_{4\,{\rm kpc}}$ erg s^{-1}, assuming a distance to the source $d = 4\ D_{4\,{\rm kpc}}$ kpc. The spectra and best-fit model are shown in Figure 4. The 2D contour plots between $N_{\rm H}$, Γ, and $F_{0.5-10\,{\rm keV}}$ are shown in Figure 5. The spectral fit results are summarized in Table 3.

We also looked for flux variability between obs. 1 and obs. 2 by leaving the normalization of the PL free to vary between the two spectra. We find a C-stat of 4212.95 for 4139 dof, and the normalizations of the two spectra are consistent with each other at the 1σ level. To establish whether the change in C-stat is statistically significant, we estimated the Bayesian information criterion (BIC) in both cases. The BIC for the case of linking the normalization of the PL, i.e., constant flux, is 4260, while the BIC for a varying PL normalization is 4255. This gives $\Delta{\rm BIC} = 5$, which implies that the case of the free PL normalization, i.e., a varying flux, is not statistically preferable over the simpler case, i.e., constant flux.

Following Y12, we also performed a spectral analysis by first modeling the background spectrum and then including its contribution to the source spectral model. Hence, we fit the background spectrum with a combination of two thermal components (for the local hot bubble and interstellar/intergalactic medium) and two PLs, one with a photon index fixed to 1.5 (assuming unresolved background active galactic nuclei, e.g., distant quasars and/or nearby low-luminosity active galactic nuclei; Porquet et al. 2004; Sazonov et al. 2008; Younes et al. 2011) and absorbed by a column density equal to the average value of the Galactic absorption toward the direction of the background region, $N_{\rm H} \approx 2.0 \times 10^{22}\,{\rm cm}^2$. The temperatures of the two thermal components are ~0.2 and ~1.1 keV, both reasonable for the thermal emission in the diffuse X-ray background (Snowden et al. 2004, 2008). We find $\Gamma \approx 0.6$ for the unabsorbed foreground PL component, which could represent some low-level solar flaring background below our exclusion threshold (Section 2). We also added Gaussian emission lines to model the instrumental lines seen in PN and MOS (see the Extended Science Analysis Software, ESAS[18]). After establishing the best-fit model to the background spectrum, we included the source spectra from the two observations and added an absorbed PL component to the total spectral model. We linked the absorption column density of the background model to that of the source. The spectral fit results for this absorbed PL component, which represents the extended emission spectral model, are summarized in Table 3. These results are in very good agreement with the results from our initial method.

Finally, we also performed the spectral fitting using the more commonly used χ^2 statistics. We binned all spectra to have a signal-to-noise ratio (S/N) of 3 and fit them with an absorbed PL, linking all parameters together. The fit is remarkably good with $\chi^2 = 153$ for 160 dof. We find a PL photon index $\Gamma = 2.1 \pm 0.3$ and an absorbing hydrogen column density $N_{\rm H} = (8.0 \pm 1.0) \times 10^{22}\,{\rm cm}^{-2}$. These results are in

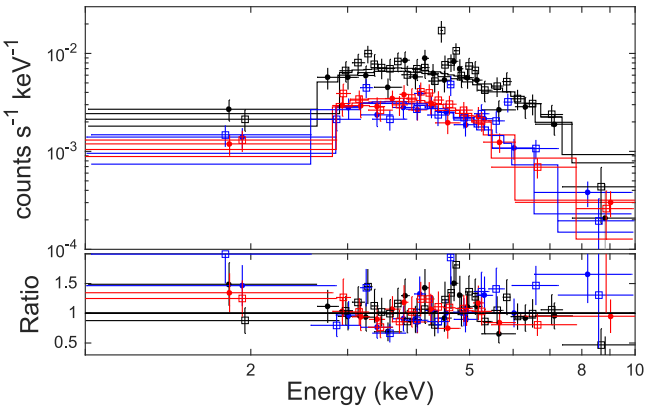

Figure 4. Upper panel: data and best-fit model of the 2014 *XMM-Newton* observations of the extended emission around Swift J1834.9−0846. The dots and open squares represent obs. 1 and obs. 2, respectively. Black, blue, and red are for PN, MOS1, and MOS2, respectively. Lower panel: data-to-model ratio. The best-fit model in this plot is obtained using C-stat; data are rebinned for clarity. See text for more details.

[17] https://heasarc.gsfc.nasa.gov/docs/xanadu/xspec/manual/XSgoodness.html

[18] http://xmm.esac.esa.int/sas/current/doc/esas/index.html

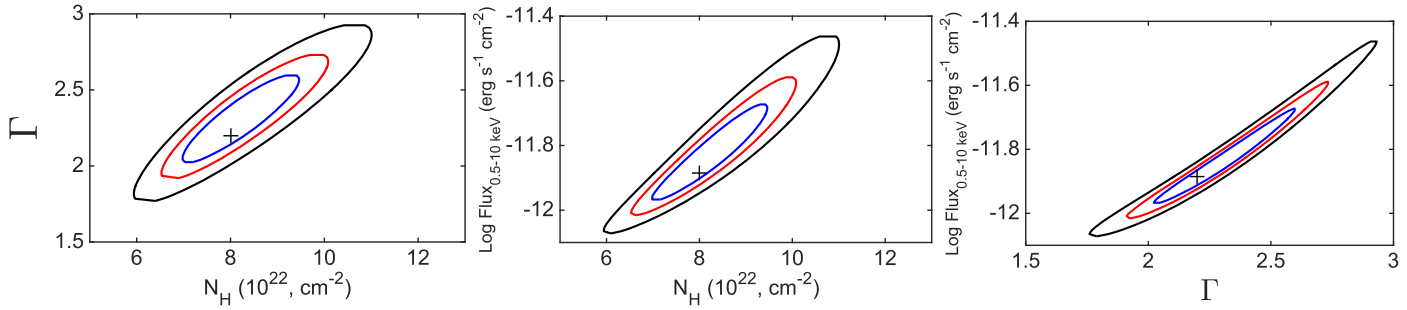

Figure 5. Left panel: $N_{\rm H}$–Γ contours. Middle panel: $N_{\rm H}$–$\log F_{0.5-10\,\rm keV}$ contours. Right panel: Γ–$\log F_{0.5-10\,\rm keV}$ contours. In all three panels, the black, blue, and red contours are at the 1σ, 2σ, and 3σ levels, respectively.

Table 3
Nebula PL Spectral Parameters

Statistic Used	$N_{\rm H}$ (10^{22} cm^{-2})	Γ	$F_{0.5-10\,\rm keV}$ (10^{-12} erg s^{-1} cm^{-2})	$L_{0.5-10\,\rm keV}$ [a] (10^{33} erg s^{-1})
C-stat[b]	$8.0^{+0.9}_{-0.8}$	2.2 ± 0.2	$1.3^{+0.4}_{-0.2}$	$2.5^{+0.7}_{-0.6}$
C-stat[c]	7.3 ± 1.0	2.1 ± 0.2	$1.1^{+0.5}_{-0.3}$	$2.1^{+1.0}_{-0.6}$
χ^2	8.0 ± 1.0	2.1 ± 0.3	$1.2^{+0.5}_{-0.2}$	$2.3^{+0.9}_{-0.5}$

Notes.
[a] Derived by adopting a 4 kpc distance.
[b] Background subtraction method.
[c] Modeled background method.

agreement with the above two methods at the 1σ confidence level. The fit parameters, along with their uncertainties, are summarized in Table 3. Using the χ^2 statistics, we also studied the case of a varying flux between the two observations. Letting the PL normalization vary freely, we find a $\chi^2 = 149$ for 159 dof. This results in an F-test statistic of 3.2 and a false-rejection probability of 8%, implying that a variable flux is not statistically favored over a constant flux.

The imaging analysis of the nebula (Figure 1) revealed a softening trend with distance from the central magnetar. To investigate this trend, we extracted the PN, MOS1, and MOS2 spectra of the two regions within the nebula as identified in Section 3.1, i.e., the inner and outer ellipses. We used C-stat in the fitting process and grouped the spectra to have 5 counts per bin. We fit the spectra simultaneously with an absorbed PL model, letting the PL normalization vary freely. As a first attempt to model the softening trend, we linked the absorption column density between the inner and the outer ellipses and let the PL index be free. This assumes that the whole extent of the nebula is equally absorbed and the softening is due to a change in the spectral curvature of the photon spectrum. This assumption leads to a good fit with C-stat of 2859.52 for 2749 dof. We find a common hydrogen column density $N_{\rm H} = (12 \pm 2) \times 10^{22}\,{\rm cm}^{-2}$. The photon indices of the inner and outer ellipses are $\Gamma_{\rm Inn} = 1.3 \pm 0.3$ and $\Gamma_{\rm Out} = 2.5 \pm 0.2$, respectively. We also tried linking the PL photon index between the inner and outer ellipses while leaving the hydrogen column density free to vary, effectively assuming that the softening is due to different absorbing column toward different parts of the nebula. We find an equally good fit with C-stat of 2862.06 for 2749 dof. We find a common PL index $\Gamma = 2.3 \pm 0.2$, while the absorption is $N_{\rm H,Inn} = (22 \pm 3) \times 10^{22}$ cm^{-2} and $N_{\rm H,Out} = (11 \pm 2) \times 10^{22}$ cm^{-2} for the inner and outer ellipses, respectively. Leaving both the absorption and the photon index free to vary does not provide any additional improvement to the fits with C-stat of 2858.97 for 2748 dof. These results are discussed in Section 4.

We checked whether an optically thin thermal component can explain the extended emission spectral properties (optically thick thermal emission is unlikely given the large size of the emission region). Using the χ^2 statistics, we fit all spectra of the whole nebula to a hot diffuse gas model (APEC in XSPEC). Fixing the abundance to solar, we find a statistically acceptable fit with χ^2 of 163 for 159 dof. We find a very high gas temperature with a 3σ lower limit $kT \gtrsim 32$ keV. Allowing the abundance to vary, we find an equally good fit with reasonable gas temperature $kT = 7^{+3}_{-1}$ keV. The abundance, however, is very low with a 3σ upper limit of <0.1 (in solar units). There are other local minima that could be found in the χ^2 space resulting in reasonable gas temperatures ($kT \sim 1$ keV) and abundances (close to solar). These fits, however, are statistically unacceptable with reduced χ^2 in the range of 1.5–1.6 for 158 dof.

3.3. Extended Emission Long-term Properties

The field of Swift J1834.9−0846 has been observed twice with *XMM-Newton* in the past, first in 2005 September and later in 2011 August, 40 days after the source went into outburst (Y12). To understand whether the extended emission varied between all *XMM-Newton* observations, we fit the 0.5–10 keV spectra of these older observations simultaneously with the 2014 observations.[19] We bin all spectra to have 5 counts per bin and use the C-stat for spectral fitting. We link all parameters together except for the PL photon indices and normalizations. This resulted in a C-stat of 4875.60 for 4677 dof. We find a hydrogen column density $N_{\rm H} = (8 \pm 1) \times 10^{22}\,{\rm cm}^{-2}$. In Figure 6, we show the $N_{\rm H}$–$\log F_{0.5-10\,\rm keV}$

[19] For the details on the spectral extraction of the 2005 and 2011 spectra, we refer the reader to Y12. We also note that the 2014 observations have significantly higher S/N compared to the 2005 and 2011 observations.

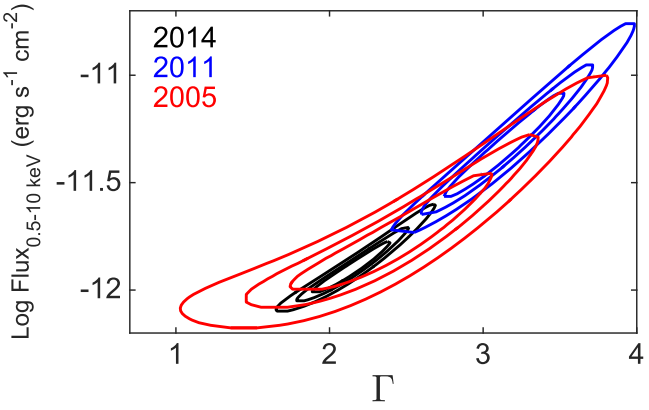

Figure 6. $N_{\rm H}$–log $F_{0.5-10\,{\rm keV}}$ 1σ, 2σ, and 3σ contours for the 2014 observations (black lines), 2011 observation (blue lines), and 2005 observation (red lines). See text for details.

contours (1σ, 2σ, and 3σ) from all three episodes (2014—black; 2011—blue; 2005—red). All observations are consistent with one another at the 3σ level. Compared to the 2005 and the 2014 observations, the 2011 observation shows, on average, a softer spectrum and a larger flux. The 2011 observation, however, was 40 days after Swift J1834.9−0846 went into outburst. The magnetar spectrum is soft during that observation ($\Gamma = 4.2$), and its high flux caused a bright, even softer, dust scattering halo detected with *XMM-Newton* (Y12), as well as with *Chandra* (Esposito et al. 2013). Hence, the 2011 extended emission spectrum is likely contaminated by these two components. We conclude that the nebula flux and spectral curvature are consistent with being constant over a span of 9 yr from 2005 to 2014.

3.4. Swift J1834.9−0846

We derived a rough estimate of the Swift J1834.9−0846 flux during obs. 1 and a 3σ upper limit during obs. 2, i.e., about 950 and 1160 days since the 2011 August outburst. Assuming an absorbed BB model with parameter values similar to the ones derived at late stages of the outburst (Esposito et al. 2013; $kT = 0.6$ keV and $N_{\rm H} = 12 \times 10^{22}$ cm^{-2}), we find a background-corrected unabsorbed 0.5–10 keV flux $F_{0.5-10\,{\rm keV}} \approx 4.0 \times 10^{-14}$ erg s^{-1} cm^{-2} and $F_{0.5-10\,{\rm keV}} \lesssim 3.0 \times 10^{-14}$ erg s^{-1} cm^{-2} for obs. 1 and obs. 2, respectively. This upper limit is comparable to the one derived by Kargaltsev et al. (2012) using a 2009 *Chandra* observation.

4. DISCUSSION

4.1. Extended Emission: Scenarios without a Wind Nebula

Dust scattering halo. Scattering of soft X-ray photons by dust in the line of sight to magnetars is a common phenomenon due to heavy absorption in their direction (e.g., Tiengo et al. 2010). The hydrogen column density toward Swift J1834.9−0846 and its surrounding extended emission is of the order of 10^{23} cm^{-2}, enough to cause a dust scattering halo in the presence of a bright illuminating source. When Swift J1834.9−0846 went into outburst in 2011 September, its flux increased by more than 3 orders of magnitude compared to its quiescent flux (Kargaltsev et al. 2012). That caused the detection of a dust scattering halo around the magnetar in *Chandra* (Esposito et al. 2013) and *XMM-Newton* (Y12). *Chandra* observations throughout the outburst indicated that the dust scattering halo suffered little delay in its flux decay compared to Swift J1834.9−0846. This placed the magnetar ~200 pc away from the dust cloud causing the halo (Esposito et al. 2013). The halo detected with *Chandra* had a size of about 30″. Emission from dust at larger angular distances from the source is expected to suffer a delay according to

$$\theta(t) \approx \left[\frac{2c}{d}\,\frac{1-x}{x}\,t\right]^{1/2}, \qquad (1)$$

where $\theta(t)$ is the off-axis angle to the observer at time t, d is the distance from the observer to the source, and $x = d_{\rm dust}/d$, where $d_{\rm dust}$ is the distance from the observer to the dust screen (Trümper & Schönfelder 1973). The observed angle θ is related to the scattering angle $\theta_{\rm scat}$ through $\theta_{\rm scat} = \theta/(1-x)$, considering that the scattering angles are usually small enough ($\theta_{\rm scat} \lesssim 10'$; Trümper & Schönfelder 1973). The flux decay from dust at a given scattering angle follows three branches, depending on the scattering grain size (a) and the energy of the incident photon (E; see Equations (8) and (9) of Svirski et al. 2011): a constant interval where the scattering is dominated by the largest grains (e.g., $a \sim 0.3$–1 μm) followed by a steep PL decay for intermediate-size grains and an exponential decay for scattering from the smallest grains (Svirski et al. 2011; Vasilopoulos & Petropoulou 2015).

Considering that $d = 4$ kpc, $d_{\rm dust} = 3.8$ kpc (based on Esposito et al. 2013) and $\theta \approx 2'$, we find a scattering angle $\theta_{\rm scat} \approx 43'$. The largest scattering angle that corresponds to the constant flux branch is approximated as $\tilde{\theta}_{\rm scat,max} = 10.4/[(E/1\,{\rm keV}) \times (a_{\rm max}/0.1\,\mu{\rm m})]$ arcminutes (Mauche & Gorenstein 1986), which, for a grain size $a = 0.3$ μm, corresponds to 3.′5. This indicates that the X-ray emission, if due to scattering from dust, is beyond the constant flux regime and in the steep PL decay regime, in contrast to the constant flux we calculate between 2011 and 2014 March and October.

Another way of looking at the problem is considering the time delay corresponding to the onset of the steep PL decay for a given scattering angle, i.e., the time over which the flux from the scattered dust is constant and dominated by scattering from the largest grains. This is given by (Svirski et al. 2011)

$$t(a_{\rm max}) \approx \frac{dx(1-x)}{2c}\,\tilde{\theta}_{\rm scat}^2 \leqslant 3.7 \times 10^3 D_{4\,{\rm kpc}} \left(\frac{E}{1\,{\rm keV}}\right)^{-2} \left(\frac{a_{\rm max}}{1\,\mu{\rm m}}\right)^{-2} {\rm s}, \qquad (2)$$

where the inequality uses the fact that $x(1-x) \leqslant 1/4$. Again, this is inconsistent with the constant flux we calculate between 2011 and 2014 March and October.

An additional argument against the dust scattering halo interpretation is the spectral shape of the extended emission. The cross section of the dust grains scales as E^{-2} of the incident photon energies (e.g., Trümper & Schönfelder 1973; Rivera-Ingraham & van Kerkwijk 2010, and references therein). Hence, for a source with a PL spectrum $E^{-\Gamma}$, illuminating a spherical dust distribution, the resulting halo spectrum scales roughly as $E^{-(\Gamma+2)}$, assuming that emission from the entire sphere is observed. The spectrum of Swift J1834.9−0846 below 10 keV at the time of the outburst was soft with $\Gamma = 3$–4, which should result in an even softer halo spectrum. Even if we assume that Swift J1834.9−0846, similar to other magnetars, possessed a hard X-ray tail above 10 keV

with $\Gamma \sim 1$ that was reprocessed by the dust sphere, a halo scattering spectrum would still be too soft to reconcile with the $\Gamma \approx 1$–2 we derive for the inner and outer rings of our extended emission. This is true when the rings were to be associated both with distinct, concentric dust spheres of different radii and with structured portions of a single scattering sphere.

Emission from the SNR W41. The mixed-morphology class of SNRs is of interest to the discussion of the extended emission seen around Swift J1834.9−0846. These represent the class of SNRs where the radio emission shows a shell-like morphology while the X-ray emission is centrally peaked (see Rho & Petre 1998; Vink 2012 for reviews and references therein). These SNRs are mostly seen in dense environments, often in the presence of molecular clouds. Interaction between these SNRs and the molecular clouds manifests through the presence of OH masers. These properties are qualitatively in agreement with the environment of the extended emission we see. The extended X-ray emission is central to the SNR W41. Analysis of CO observations indicates a considerable amount of molecular material in this direction, and OH masers have been reported, indicating the possible interaction of the cloud with the SNR (Frail et al. 2013). However, the X-ray emission from this class of SNRs is purely thermal, with an average temperature of about 0.6 keV, and their X-ray spectra show strong emission lines from metal-rich plasma, in contrast with the featureless, nonthermal spectrum of the extended emission we see here. Moreover, these SNRs are usually younger than the 10^5 yr estimated age of W41 (Tian et al. 2007). Finally, while centrally peaked, the X-ray emission from these SNRs is generally present throughout the radio shell albeit at lower surface brightness (Rho & Petre 1998). The extended emission we observe is detected at a very small volume compared to the SNR W41 volume, only at the position of and around the magnetar Swift J1834.9−0846. Hence, the X-ray extended emission we observe here is inconsistent with a mixed-morphology SNR origin.

X-ray reflection nebula. GMCs in the Galactic center region emit X-ray radiation that is thought to be the reflection of past activity from the supermassive black hole Sgr A* a few hundred years ago (e.g., Ponti et al. 2010). The observational properties of the X-ray emission from these clouds are a hard 2–10 keV spectrum with a photon index $\Gamma \approx 1.0$ and a broad (equivalent width of ∼1 keV) neutral or low-ionized fluorescent Fe K emission line with a flux proportional to the flux of the illuminating source (Sunyaev & Churazov 1998). Moreover, the X-ray flux from these GMCs is typically observed to vary on timescales of years (e.g., Ponti et al. 2010). This variability is more pronounced if the energy in the illuminating source is the result of a brief intense flare compared to a steady output (Sunyaev & Churazov 1998). Similar results are derived for other GMCs with different illuminating sources (e.g., Sekimoto et al. 2000; Corcoran et al. 2004). Hence, a past strong bursting episode and/or a giant flare (GF) from Swift J1834.9−0846 could in principle result in an X-ray-reflected spectrum from the GMC in its direction. However, the X-ray photon index of our extended emission, $\Gamma = 2.2$, is much larger than the hard X-ray spectrum expected from reflection. Assuming similar properties between the GMC in the direction of Swift J1834.9−0846 and the ones in the Galactic center, a strong bursting episode or outburst from the source should give rise to a strong Fe K line, which we do not detect in the current observation. Moreover, we do not observe any variability in a span of 9 yr, while variability on timescales of a few years has been reported for the GMC in the Galactic center region (Ponti et al. 2010; Terrier et al. 2010). Finally, assuming reflection from the GMC, it is hard to reconcile the small angular size of our extended emission with the angular size of the cloud that is a few times larger (Tian et al. 2007; Esposito et al. 2010). We conclude that a reflection scenario is inconsistent with the X-ray observational properties of the extended emission we detect around Swift J1834.9−0846.

Emission from a background galaxy cluster. In the X-ray band, galaxy clusters are observed as extended sources with spectra best fit by optically thin thermal models. The gas responsible for their X-ray emission is mostly found to have a temperature of the order of a few keV and abundances in the range of ∼0.4–1.0 solar (e.g., White 2000; Maughan et al. 2008). While most of these galaxy clusters are seen outside the Galactic plane, Townsley et al. (2011) discovered a galaxy cluster in the Galactic plane (Galactic latitude $l \sim -1\overset{\circ}{.}2$). Compared to the galaxy cluster class, the unusually high temperature ($kT \gtrsim 32$ keV, assuming solar abundance) we derive when fitting the extended emission around the magnetar with a thermal model is inconsistent with the temperatures of other clusters. Moreover, allowing the abundance to vary, the very low value we derive (<0.1, 3σ confidence) is also inconsistent with most clusters (even when we consider the different abundance values at different redshifts). We therefore exclude the possibility that the extended X-ray emission around Swift J1834.9−0846 is due to a background galaxy cluster.

4.2. A Magnetar Wind Nebula

The asymmetric morphology of the extended emission we detect around Swift J1834.9−0846, its nonthermal origin with an X-ray PL photon index $\Gamma \approx 2$ and with a surface brightness peaking at the *Chandra* position of the central object (Kargaltsev et al. 2012), and its flux constancy over a 9 yr period closely resemble the properties of a number of typical PWNs around RPPs (see, e.g., Kargaltsev & Pavlov 2008; Kargaltsev et al. 2013; Bamba et al. 2010). The central object in our case, however, is a typical magnetar source. Hence, given that it appears unlikely that this extended emission is the result of dust scattering, emission from W41, reflection, or a background galaxy cluster, we conclude that the 2014 *XMM-Newton* data, combined with the two earlier observations, unambiguously confirm our earlier results (Y12) that the extended emission around Swift J1834.9−0846 is the first manifestation of a wind nebula around a typical magnetar.

The timing properties of the magnetar result in a rotational energy loss $\dot{E}_{\rm rot} = 2.1 \times 10^{34}\,{\rm erg\,s^{-1}}$. Assuming that the X-ray nebula is powered by the magnetar rotational energy, this translates into an unusually high X-ray efficiency $\eta_{\rm X} = L_{\rm X,PWN}/\dot{E}_{\rm rot} = 0.1$.

Compared to the PWN around the high-B RPP PSR J1846–0258, the wind nebula around Swift J1834.9−0846 seems markedly different, with the only shared observational characteristic being the X-ray spectral curvature with a common photon index $\Gamma = 2.0$ (Ng et al. 2008). The size of the PWN around PSR J1846–0258 is a few tens of arcseconds, an order of magnitude smaller than the size of the wind nebula around Swift J1834.9−0846. Its X-ray efficiency of about 2%, while at the high end of PWN/RPP systems, is 5 times smaller than the case of Swift J1834.9−0846. The observational

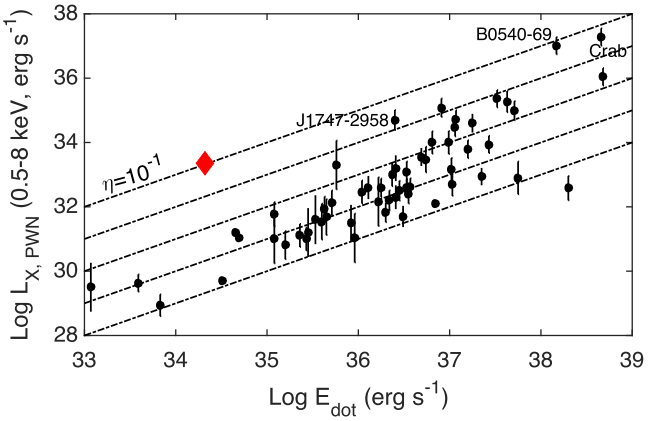

Figure 7. PWN X-ray luminosity as a function of the rotational energy loss of their powering pulsar. Black dots are RPPs with properties taken from Kargaltsev et al. (2013). The dot-dashed lines correspond to constant X-ray efficiencies from 10^{-1} down to 10^{-5} (top to bottom) of converting the rotational power to PWN X-ray luminosity. The red diamond corresponds to the value derived for the wind nebula around the magnetar Swift J1834.9−0846. The names of three other PWN/RPP systems are indicated, of which B0540-69 and Crab share the same high efficiency as the wind nebula around the magnetar. All data points include a statistical as well as a systematic error in their wind nebula X-ray luminosity (assumed 40%). For the magnetar this is represented by the size of the diamond. No error is shown on $E_{\rm dot}$. Figure adapted from Kargaltsev et al. (2013).

properties of the PWN around PSR J1846–0258 seem to indicate a typical rotation-powered PWN in a young system (spin-down age $\tau \approx 800$ yr), in contrast to Swift J1834.9−0846.

Wind nebulae around other high-B sources have also been suggested. Camero-Arranz et al. (2013; see also Rea et al. 2009) discussed the case of the extended emission around RRAT J1819−1458 ($B \approx 5.0 \times 10^{13}$ G). Its spectrum can be well modeled by a PL with a photon index $\Gamma \approx 3.5$, much softer than typical PWNs and the wind nebula around Swift J1834.9−0846. Assuming a nebula origin for the extended emission, a high X-ray efficiency of about 15% is required. Recently, Israel et al. (2016) hinted at the possibility of a wind nebula around the newly discovered magnetar SGR J1935+2154 during outburst ($B \approx 2.2 \times 10^{14}$ G). The extended emission is well modeled by a PL with a soft spectrum, $\Gamma \approx 3.0$, and its X-ray efficiency is about 35%, both larger than the case of Swift J1834.9−0846. We note, however, that in the above two cases, the current available data are insufficient to draw any firm conclusions on the true nature of these two extended emissions, and a dust scattering halo interpretation is still a viable explanation.

Figure 7 shows the X-ray luminosity of PWNs as a function of the rotational energy loss of their powering pulsar, while the magnetar is indicated with a red diamond. Only two PWN/RPP systems come close to the high efficiency of Swift J1834.9−0846: the Crab pulsar and B0540−69, which is also known as the "Crab twin." However, both sources are much younger, with spin-down ages of 1.3 and 1.6 kyr, respectively, compared to $\tau = 4.9$ kyr for the magnetar (the discrepancy is more pronounced if we assume that Swift J1834.9−0846 is associated with the SNR W41 with an estimated age of $\gtrsim$50 kyr). Another interesting source to mention in this regard is the PWN/RPP system PSR J1747−2958 (Gaensler et al. 2004), which has an estimated age of ∼25 kyr and an X-ray efficiency $\eta = 0.02$, which are a factor of 5 larger and lower than the age and efficiency we derive for Swift J1834.9−0846, respectively. There are differences between the two systems, nonetheless. The PWN around PSR J1747−2958 is a prominent nebula in radio (Gaensler et al. 2004), in contrast to the wind nebula we see here (Kargaltsev et al. 2012), while its rotational energy $\dot{E}$ is more than 2 orders of magnitude larger. In fact, Figure 7 shows that all the PWN/RPP systems with $\dot{E}$ within an order of magnitude of the value for Swift J1834.9−0846 have X-ray efficiencies at least two orders of magnitude lower.

Another unusual property of this wind nebula around Swift J1834.9−0846 is the extremely high ratio of the nebula X-ray luminosity to the luminosity of the central magnetar in quiescence, $L_{\rm X,PWN}/L_{\rm X,magnetar} \gtrsim 40$. Kargaltsev et al. (2007; see also Kargaltsev & Pavlov 2008) found that this ratio is tightly clustered around 4 for almost all PWN/RPP systems, regardless of efficiency and age. This value is an order of magnitude lower than the one we derive here. This high brightness could be the effect of its collision with the W41 SNR reverse shock (assuming connection between the two). As is shown in Gelfand et al. (2009), the compression of the nebula by the reverse shock tends to increase its particle and magnetic energy, as well as the strength of its magnetic field. This tends to rapidly increase the nebula synchrotron luminosity.

An alternative possibility for the unusual high efficiency and brightness in the wind nebula around Swift J1834.9−0846 is that there might be an extra source of power in addition to the rotational energy of the magnetar. This extra source of power is most likely the decay of the magnetar's ultrastrong magnetic field, with an inferred surface dipole magnetic field of $B = 2.1 \times 10^{14}$ G. Particle outflows, either steady or released during bursting episodes, could be driven out from the magnetar as Alfvén waves (Thompson & Blaes 1998; Harding et al. 1999; Tong et al. 2013). The best observational evidence is from the transient radio nebulae detected from the magnetars SGR 1900+14 and SGR 1806−20 following their respective 1998 and 2004 GFs (Frail et al. 1999; Gaensler et al. 2005; Gelfand et al. 2005; Taylor et al. 2005; Granot et al. 2006). It is obvious that the nebula we see around Swift J1834.9−0846 is steady over a minimum of a 9 yr period and hence intrinsically different from the radio nebulae seen around SGR 1900+14 and SGR 1806−20 following the GFs. Particle outflows in magnetars, however, are not restrained to GF emission and are expected during regular bursting episodes (Thompson & Duncan 1996; Gill & Heyl 2010), particularly given that the magnetic Eddington limit is low enough that it can be breached even by the short bursts (Watts et al. 2010; van Putten et al. 2013). Indeed, the strong torque changes seen in many magnetars point toward a particle wind escaping out through open field lines out to (at least) the light cylinder (Kaspi et al. 2014; Archibald et al. 2015; Younes et al. 2015). Moreover, the discovery of quasi-periodic oscillations in the short-recurring bursts of magnetars points to Alfvén waves driven by ongoing seismic activity (Huppenkothen et al. 2014a, 2014b). Harding et al. (1996) studied the case of particle outflow following short magnetar bursts and found that the cooling timescale is very long (compared to the time between bursts) such that the nebular emission is steady rather than transient, in agreement with our results.

The above qualitative theoretical reasoning raises the question about why would Swift J1834.9−0846 be the only magnetar so

far powering a wind nebula, given that previous searches around individual magnetars have returned no sign of extended emission attributable to wind nebulae (e.g., Viganò et al. 2014). With only one observed so far, it is difficult to draw any firm conclusions. Nevertheless, Swift J1834.9−0846 has some interesting characteristics that are not shared with the entire magnetar population. First, the environment of Swift J1834.9−0846 is extremely crowded, with a *Fermi* GeV source, an H.E.S.S. TeV source, an SNR, a GMC, and an OH maser in its vicinity (Frail et al. 2013; H.E.S.S. Collaboration et al. 2015). The relationship between all these sources is unclear. However, it is tempting to speculate that environmental effects from such a rich field could be playing a role in the production of this wind nebula (e.g., triggering of pair cascade by external gamma rays from a nearby source; Shukre & Radhakrishnan 1982; Istomin and Sob'yanin 2011). Second, the Swift J1834.9−0846 X-ray luminosity in quiescence is $L_{\rm X} = 5 \times 10^{31}\, D_{4\rm kpc}^2\, {\rm erg\ s^{-1}}$. Only five other magnetars (SGR 0418+5729, SGR 1745−2900, XTE J1810−197, Swift J1822.3−1606, 3XMM J185246.6+003317)[20] have luminosities $\lesssim 10^{32}$ erg s^{-1}. Among these five, three have the smallest surface B fields measured (SGR 0418+5729, Swift J1822.3−1606, 3XMM J185246.6+003317; $B < 4 \times 10^{13}$ G), and only one source, SGR 1745−2900, has a rotational energy loss rate $\dot{E}$ similar to Swift J1834.9−0846, while the rest have $\dot{E}$ at least an order of magnitude lower. Hence, from an observational point of view, it seems that the combination of very weak X-ray luminosity, a magnetar-like B-field strength, and a somewhat large $\dot{E}$ (properties that are only shared by the Galactic center magnetar SGR 1745−2900) may favor wind nebula production. Another possibility is that the Swift J1834.9−0846 magnetar/nebula system is an older analog to the Kes 75 system, where the central pulsar evolves into a magnetar while preserving its originial PWN.

Finally, we briefly discuss the softening trend within the Swift J1834.9−0846 nebula (see Section 3.2). While the usual cause for spectral differences within wind nebulae around pulsars is a change in spectral curvature rather than absorption, the latter scenario should be considered in our case. The heavy absorption for Swift J1834.9−0846 is thought to be due to the existence of a GMC in its direction (Tian et al. 2007). The densities within these clouds could be nonuniform, causing spatially variable absorption. The magnetar, surrounded by the inner nebula, was a bright X-ray point source in 2011 when in outburst. The *XMM-Newton* spectrum was fit in Y12 with an absorbed PL ($N_{\rm H} = (24 \pm 1) \times 10^{22}\,{\rm cm^{-2}}$) and an absorbed blackbody (BB, $N_{\rm H} = (13 \pm 1) \times 10^{22}\,{\rm cm^{-2}}$). Y12 found that the absorbed BB fit ($\chi^2_\nu = 1.04$ for 232 dof) was superior to the PL fit ($\chi^2_\nu = 1.15$ for 232 dof), possibly indicating that the true absorption toward the magnetar, and by extrapolation the inner nebula, is similar to the absorption toward the outer nebula. This potentially points to a change in the photon index as the primary cause for the spectral softening that we see in our data, strengthening the case for a typical wind nebula around Swift J1834.9−0846, similar to PWNs around young pulsars. Such a softening trend could be attributed to synchrotron burnoff of energetic particles. This conclusion, however, requires a deeper X-ray observation to firmly confirm it and/or a theoretically motivated spectral modeling (i.e., whether emission from marginally fast cooling electrons with a given initial PL energy distribution could quantitatively explain the spectral softening observed).

[20] http://www.physics.mcgill.ca/ pulsar/magnetar/main.html

5. CONCLUSION

In this paper, we studied two deep *XMM-Newton* observations of the extended emission around the magnetar Swift J1834.9−0846. The observations, separated by 7 months, were taken in 2014 March and October, 2.5 and 3.1 yr after the source went into outburst. The magnetar is weakly detected in the first observation, while it faded below the detection limit during the second one. The extended emission is clearly detected in both observations; it is best described with a nonthermal PL model with a photon index $\Gamma \approx 2.2 \pm 0.2$. Fitting these spectra with archival ones taken 3 and 9 yr earlier, we find that the flux and spectral curvature of the extended emission are constant with $F_{0.5-10\,\rm keV} \approx 1.1 \times 10^{-12}$ erg cm^{-2} s^{-1}. This provides a strong observational case confirming the Y12 results that Swift J1834.9−0846 is indeed the first magnetar to show a surrounding wind nebula. Our results imply that these properties are likely no longer exclusive to RPPs, and they further narrow the gap between these two subpopulations of isolated NSs. A more in-depth theoretical interpretation of these results will be presented in a separate accompanying paper.

Based on observations obtained with *XMM-Newton*, an ESA science mission with instruments and contributions directly funded by ESA Member States and NASA. A.L.W. acknowledges support from NWO Vidi Grant No. 639.042.916. O.J.R. acknowledges support from Science Foundation Ireland under Grant No. 12/IP/1288. C.K. and G.Y. acknowledge support by NASA through grant NNH07ZDA001-GLAST (PI: C. Kouveliotou). G.Y. thanks Dale Frail for insightful discussions on this project. We thank the referee for useful comments that improved the quality of the manuscript. J.G. and R.G. acknowledge support from the Israeli Science Foundation under Grant No. 719/14. R.G. is supported by an Outstanding Postdoctoral Researcher Fellowship at the Open University of Israel.

REFERENCES

Archibald, R. F., Kaspi, V. M., Ng, C.-Y., et al. 2015, ApJ, 800, 33
Arnaud, K. A. 1996, in ASP Conf. Ser. 101, Astronomical Data Analysis Software and Systems V, ed. G. H. Jacoby, & J. Barnes (San Francisco, CA: ASP), 17
Asai, K., Dotani, T., Hoshi, R., et al. 1998, PASJ, 50, 611
Bamba, A., Anada, T., Dotani, T., et al. 2010, ApJL, 719, L116
Beloborodov, A. M. 2009, ApJ, 703, 1044
Camero-Arranz, A., Rea, N., Bucciantini, N., et al. 2013, MNRAS, 429, 2493
Camilo, F., Ransom, S. M., Halpern, J. P., et al. 2006, Natur, 442, 892
Camilo, F., Ransom, S. M., Halpern, J. P., & Reynolds, J. 2007, ApJL, 666, L93
Campana, S., Colpi, M., Mereghetti, S., Stella, L., & Tavani, M. 1998, A&ARv, 8, 279
Corcoran, M. F., Hamaguchi, K., Gull, T., et al. 2004, ApJ, 613, 381
Dall'Osso, S., Granot, J., & Piran, T. 2012, MNRAS, 422, 2878
Esposito, P., Israel, G. L., Turolla, R., et al. 2010, MNRAS, 405, 1787
Esposito, P., Tiengo, A., Rea, N., et al. 2013, MNRAS, 429, 3123
Frail, D. A., Claussen, M. J., & Méhault, J. 2013, ApJL, 773, L19
Frail, D. A., Kulkarni, S. R., & Bloom, J. S. 1999, Natur, 398, 127
Gaensler, B. M., Kouveliotou, C., Gelfand, J. D., et al. 2005, Natur, 434, 1104
Gaensler, B. M., & Slane, P. O. 2006, ARA&A, 44, 17
Gaensler, B. M., van der Swaluw, E., Camilo, F., et al. 2004, ApJ, 616, 383
Gavriil, F. P., Gonzalez, M. E., Gotthelf, E. V., et al. 2008, Sci, 319, 1802
Gelfand, J. D., Lyubarsky, Y. E., Eichler, D., et al. 2005, ApJL, 634, L89
Gelfand, J. D., Slane, P. O., & Zhang, W. 2009, ApJ, 703, 2051

Gill, R., & Heyl, J. S. 2010, MNRAS, 407, 1926
Gotthelf, E. V., Vasisht, G., Boylan-Kolchin, M., & Torii, K. 2000, ApJL, 542, L37
Granot, J., Ramirez-Ruiz, E., Taylor, G. B., et al. 2006, ApJ, 638, 391
Harding, A. K. 1996, in AIP Conf. Ser. 366, High Velocity Neutron Stars, ed. R. E. Rothschild, & R. E. Lingenfelter (Melville, NY: AIP), 118
Harding, A. K., Contopoulos, I., & Kazanas, D. 1999, ApJL, 525, L125
H.E.S.S. Collaboration, Abramowski, A., Aharonian, F., et al. 2015, A&A, 574, A27
Huppenkothen, D., D'Angelo, C., Watts, A. L., et al. 2014a, ApJ, 787, 128
Huppenkothen, D., Heil, L. M., Watts, A. L., & Göğüş, E. 2014b, ApJ, 795, 114
Israel, G. L., Esposito, P., Rea, N., et al. 2016, MNRAS, 457, 3448
Istomin, Y. N., & Sob'yanin, D. N. 2011, JETP, 113, 592
Kargaltsev, O., Kouveliotou, C., Pavlov, G. G., et al. 2012, ApJ, 748, 26
Kargaltsev, O., & Pavlov, G. G. 2008, in AIP Conf. Ser. 983, 40 Years of Pulsars: Millisecond Pulsars, Magnetars and More, ed. C. Bassa et al. (Melville, NY: AIP), 171
Kargaltsev, O., Pavlov, G. G., & Garmire, G. P. 2007, ApJ, 660, 1413
Kargaltsev, O., Rangelov, B., & Pavlov, G. G. 2013, arXiv
Kaspi, V. M., Archibald, R. F., Bhalerao, V., et al. 2014, ApJ, 786, 84
Kaspi, V. M., Roberts, M. S. E., & Harding, A. K. 2006, in Compact Stellar X-ray Sources, ed. W. H. G. Lewin, & M. van der Klis (Cambridge: Cambridge University Press)
Leahy, D. A., & Tian, W. W. 2008, AJ, 135, 167
Livingstone, M. A., Kaspi, V. M., Gotthelf, E. V., & Kuiper, L. 2006, ApJ, 647, 1286
Mauche, C. W., & Gorenstein, P. 1986, ApJ, 302, 371
Maughan, B. J., Jones, C., Forman, W., & Van Speybroeck, L. 2008, ApJS, 174, 117
Mereghetti, S., Pons, J. A., & Melatos, A. 2015, SSRv, 191, 315
Ng, C.-Y., Slane, P. O., Gaensler, B. M., & Hughes, J. P. 2008, ApJ, 686, 508
Olausen, S. A., & Kaspi, V. M. 2014, ApJS, 212, 6
Ponti, G., Terrier, R., Goldwurm, A., Belanger, G., & Trap, G. 2010, ApJ, 714, 732
Porquet, D., Reeves, J. N., O'Brien, P., & Brinkmann, W. 2004, A&A, 422, 85
Rea, N., Esposito, P., Turolla, R., et al. 2010, Sci, 330, 944
Rea, N., Israel, G. L., Pons, J. A., et al. 2013, ApJ, 770, 65
Rea, N., McLaughlin, M. A., Gaensler, B. M., et al. 2009, ApJL, 703, L41
Rea, N., Pons, J. A., Torres, D. F., & Turolla, R. 2012, ApJL, 748, L12
Rho, J., & Petre, R. 1998, ApJL, 503, L167
Rivera-Ingraham, A., & van Kerkwijk, M. H. 2010, ApJ, 710, 797
Sazonov, S., Krivonos, R., Revnivtsev, M., Churazov, E., & Sunyaev, R. 2008, A&A, 482, 517
Sekimoto, Y., Matsuzaki, K., Kamae, T., et al. 2000, PASJ, 52, L31
Shukre, C. S., & Radhakrishnan, V. 1982, ApJ, 258, 121
Snowden, S. L., Collier, M. R., & Kuntz, K. D. 2004, ApJ, 610, 1182
Snowden, S. L., Mushotzky, R. F., Kuntz, K. D., & Davis, D. S. 2008, A&A, 478, 615
Strüder, L., Briel, U., Dennerl, K., et al. 2001, A&A, 365, L18
Sunyaev, R., & Churazov, E. 1998, MNRAS, 297, 1279
Svirski, G., Nakar, E., & Ofek, E. O. 2011, MNRAS, 415, 2485
Taylor, G. B., Gelfand, J. D., Gaensler, B. M., et al. 2005, ApJL, 634, L93
Terrier, R., Ponti, G., Bélanger, G., et al. 2010, ApJ, 719, 143
Thompson, C., & Blaes, O. 1998, PhRvD, 57, 3219
Thompson, C., & Duncan, R. C. 1995, MNRAS, 275, 255
Thompson, C., & Duncan, R. C. 1996, ApJ, 473, 322
Thompson, C., Lyutikov, M., & Kulkarni, S. R. 2002, ApJ, 574, 332
Tian, W. W., Li, Z., Leahy, D. A., & Wang, Q. D. 2007, ApJL, 657, L25
Tiengo, A., Vianello, G., Esposito, P., et al. 2010, ApJ, 710, 227
Tong, H., Xu, R. X., Song, L. M., & Qiao, G. J. 2013, ApJ, 768, 144
Torne, P., Eatough, R. P., Karuppusamy, R., et al. 2015, MNRAS, 451, L50
Townsley, L. K., Broos, P. S., Corcoran, M. F., et al. 2011, ApJS, 194, 1
Trümper, J., & Schönfelder, V. 1973, A&A, 25, 445
Turolla, R., Zane, S., & Watts, A. L. 2015, RPPh, 78, 116901
van der Horst, A. J., Connaughton, V., Kouveliotou, C., et al. 2010, ApJL, 711, L1
van Putten, T., Watts, A. L., D'Angelo, C. R., Baring, M. G., & Kouveliotou, C. 2013, MNRAS, 434, 1398
Vasilopoulos, G., & Petropoulou, M. 2015, arXiv
Verner, D. A., Ferland, G. J., Korista, K. T., & Yakovlev, D. G. 1996, ApJ, 465, 487
Viganò, D., Rea, N., Esposito, P., et al. 2014, JHEAp, 3, 41
Vink, J. 2012, A&ARv, 20, 49
Watts, A. L., Kouveliotou, C., van der Horst, A. J., et al. 2010, ApJ, 719, 190
White, D. A. 2000, MNRAS, 312, 663
Wilms, J., Allen, A., & McCray, R. 2000, ApJ, 542, 914
Younes, G., Kouveliotou, C., Kargaltsev, O., et al. 2012, ApJ, 757, 39
Younes, G., Kouveliotou, C., & Kaspi, V. M. 2015, ApJ, 809, 165
Younes, G., Porquet, D., Sabra, B., & Reeves, J. N. 2011, A&A, 530, A149